Meas. Sci. Technol. **19** (2008) 125503 (10pp) doi:10.1088/0957-0233/19/12/125503

On the improvement of two-dimensional curvature computation and its application to turbulent premixed flame correlations

R S M Chrystie[1], I S Burns[1], J Hult[1] and C F Kaminski[1,2]

[1] Department of Chemical Engineering and Biotechnology, University of Cambridge, Pembroke Street, Cambridge, CB2 3RA, UK
[2] SAOT School of Advanced Optical Technologies, Max Planck Research Group, Division III, Universität Erlangen-Nürnberg, Germany

E-mail: rsmc3@cam.ac.uk and cfk23@cam.ac.uk

Received 29 May 2008, in final form 16 September 2008
Published 24 October 2008
Online at stacks.iop.org/MST/19/125503

Abstract
Measurement of curvature of the flamefront of premixed turbulent flames is important for the validation of numerical models for combustion. In this work, curvature is measured from contours that outline the flamefront, which are generated from laser-induced fluorescence images. The contours are inherently digitized, resulting in pixelation effects that lead to difficulties in computing curvature of the flamefront accurately. A common approach is to fit functions locally to short sections along the flame contour, and this approach is also followed in this work; the method helps smoothen the pixelation before curvature is measured. However, the length and degree of the polynomial, and hence the amount of smoothing, must be correctly set in order to maximize the precision and accuracy of the curvature measurements. Other researchers have applied polynomials of different orders and over different segment lengths to circles of known curvature as a test to determine the appropriate choice of polynomial; it is shown here that this method results in a sub-optimal choice of polynomial function. Here, we determine more suitable polynomial functions through use of a circle whose radius is sinusoidally modulated. We show that this leads to a more consistent and reliable choice for the local polynomial functions fitted to experimental data. A polynomial function thus determined is then applied to flame contour data to measure curvature of experimentally acquired flame contours. The results show that there is an enhancement in local flame speed at sections of the flamefront with a non-zero curvature, and this agrees with numerical models.

Keywords: flamefront curvature, laser-induced fluorescence, polynomial fitting

1. Introduction

To further the understanding of the behaviour of turbulent premixed flames within various technical combustions devices, fundamental understanding needs to be acquired from experiments on a laboratory scale. The element of the flame of greatest interest in such studies is the flamefront, comprising a thin (usually less than 0.5 mm thick) region in the flame, that separates reactants from the burnt products. The rapid exothermic reactions between fuel and oxygen characteristic of flames take place in the flamefront. In weakly turbulent flames, where extinction is negligible, the flamefront is continuous in space (Veynante and Vervisch 2002). Here we study weakly turbulent flames, in which the flamefront adopts a distorted (wrinkled) profile that evolves in time. It is this distortion that leads to curvature of the flamefront and it is caused by the presence of vortices within the turbulent gaseous mixture of the flame. These vortices continuously rotate and translate in space, and some impinge onto the flamefront consequently wrinkling its configuration (Rutland and Ferziger 1991).

The significance of flamefront curvature arises because it appears to have a profound effect on the overall reaction

rate between fuel and oxygen. On one hand, curvature leads to strain upon the flamefront (Veynante and Vervisch 2002), which in turn leads to an increased flame surface area and hence a larger global rate of reaction. Curvature of the flamefront also impacts on reaction rates through induction of the thermodiffusive effect (Williams 1986). The relationship between the local rate of burning and flamefront curvature is governed by the global Lewis number ($Le = \alpha/D$), where α is the thermal diffusivity of the fuel–air mixture and D is the binary mass diffusivity of the fuel in nitrogen at inlet conditions (Law 1988, Rutland and Trouvé 1993); this dimensionless number plays an important role in determining the behaviour of the flame. From an engineering perspective, precise knowledge of the underlying phenomenon affecting reaction rates is crucial, in order to optimize the design of combustion units and better control their operability. Numerical modelling, together with experimentation, plays an increasing role in these efforts. The numerical models of engineering utility, e.g., large eddy simulations (LES), make assumptions to achieve closure of the governing equations (Pitsch 2006). Reliable empirical data are required to refine and validate these models, and this forms the motivation for this study.

The effect of curvature on the local rate of reaction has been subject of a previous experimental study by the current group (Ayoola *et al* 2006). These efforts were based on the simultaneous measurement of CH_2O and OH radical concentration distributions in a flame using planar laser-induced fluorescence (PLIF). The measurements enabled the flamefront to be reliably isolated, as well as a local resolution of the rate of heat release (rate of reaction) at the flamefront to be made; details of how these quantities were extracted are outlined later in this paper. The correlations generated between the local rate of heat release and curvature exhibited, however, only a little negative correlation (if indeed any), which was not in agreement with results obtained from direct numerical simulations (DNS) of similar flames studied by Chakraborty and Cant (2005) and Rutland and Trouvé (1993). In the work of Ayoola *et al* (2006), curvature was computed directly from the raw data of the experiments. The computations were performed by first extracting the contour of the flamefront, as delineated by the local maximum of the gradient of the intensity in OH PLIF images of the flame, and then measuring the curvature directly from the pixelated flame contours by calculating the spatial first and second derivatives using the discrete pixel-based coordinates of the flame contour.

Flame contours, thus obtained, are inherently pixelated and their jagged profile requires smoothing to improve precision of measured curvature, since the computation of the second derivative is especially sensitive to pixelation-induced noise. The smoothing can be achieved by employing either Fourier spatial filtering (Gashi *et al* 2005, Chen 2007) or local polynomial curve fitting (Kostiuk *et al* 1999, Shy *et al* 1999, Renou *et al* 2000, Haq *et al* 2002, Soika *et al* 2003). Both spatial filtering methods require tuning of their parameters to control the degree of smoothing, such that curvature can be computed with a minimal error. This is done by applying the filtering algorithm to a pixelated theoretical test curve and then varying the filtering parameters to minimize the difference between measured and theoretical curvatures. The test curve is a line that is defined by a theoretical function, whose curvature can be obtained analytically. The measured curvature is obtained by creating a pixelated representation of the test curve. An important point is that this must be done using pixels of a size corresponding to the projection of a pixel of the camera used during the experiment onto the object plane in the flame being imaged. Thus, the choice of spatial filtering parameters depends on the spatial resolution of the PLIF images; however they also depend on the properties of the flame under study (subject to different levels of strain rate and turbulence, for instance). To a certain degree the choice can also be affected by experimental parameters, such as the signal to noise ratio of the PLIF images and any artefacts introduced by incorrect laser sheet profile corrections. Here, we address one part of the problem in resolving curvatures adequately in flamefronts by matching the type of polynomial to the object being measured. For polynomial fitting, there is currently no systematic method for choosing these parameters. Test circles of various radii have been used, for instance (Haq *et al* 2002). In this paper, we show how critically the final accuracy and precision of the measured flamefront curvature depend on the correct choice of test curve.

The aims of this work are to improve the accuracy and precision of curvature measurements from digitized flame contours by developing a more systematic method for computing curvature using local polynomial curve fitting. The contents of this paper are organized as follows. The details of the original experimental setup of Ayoola *et al* (2006) are briefly described here. The particulars of the polynomial fitting method are then detailed. The results from the various test curves' parameters and their application to the flamefront data are presented and discussed. The data of Ayoola are then reanalysed using our improved methods and the improved accuracy, and precision obtained demonstrates that indeed correlations are present that were buried in noise by which conventional methods are affected.

2. Experimental details

2.1. Burner system

An ethylene/air flame was stabilized on a counterflow burner (Ayoola *et al* 2006), which is represented in figure 1. Flow rates were regulated using mass flow controllers, to produce a lean flame with equivalence ratio of $\phi = 0.55$. Effects of air entrainment near the edge of the flame were minimized by the presence of a nitrogen coflow. The turbulent flame was stabilized in the central plane between two opposing nozzles using bulk gas flow velocities of equal magnitude. Turbulence-generating grids and flow straighteners were used to create a uniform turbulent velocity profile at the nozzle's exit planes; the combustor is similar to that described by Mastorakos *et al* (1992). Three flow speeds were used in the study namely 2.4, 2.9 and 3.4 m s^{-1} corresponding to bulk strain rates of 137, 166 and 194 s^{-1}, respectively. The flames were in the 'wrinkled and stretched flamelets' regime and the highest strain rate flames operated close to the extinction limit.

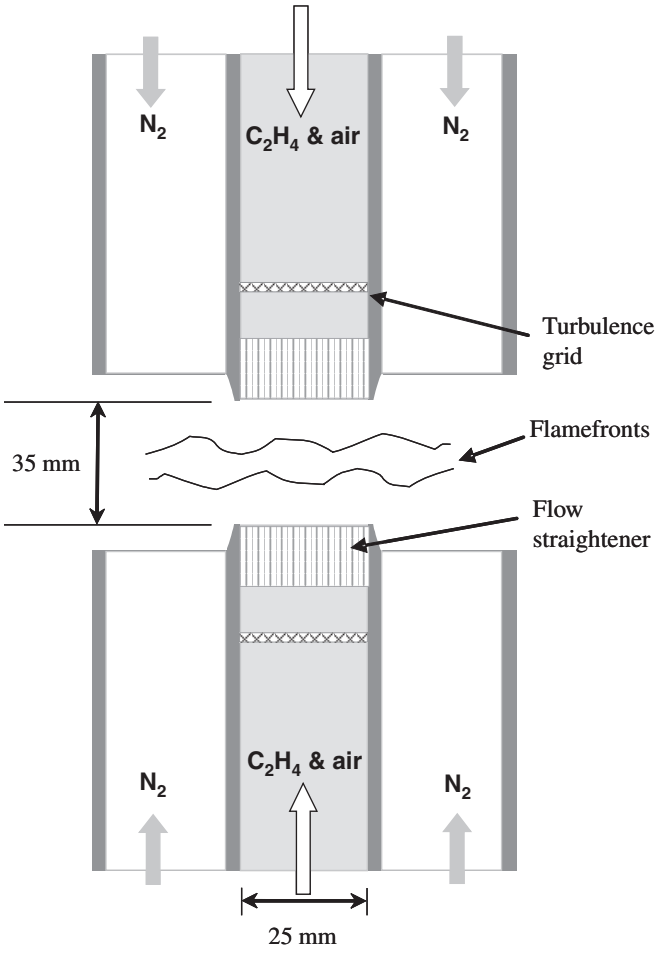

Figure 1. Schematic of the counterflow burner cross-section.

2.2. Laser diagnostics

The PLIF images were generated using two Nd:YAG lasers (Continuum Surelite), two dye lasers (Sirah CobraStretch) and two high-resolution double exposure ICCD cameras (Lavision Nanostar). The camera for imaging OH LIF was fitted with a UV f/4.5 camera lens (Nikkor) with UG 11 and WG 305 filters (Comar) attached. The CH_2O camera was fitted with an f/1.2 camera lens (Nikkor) and GG 375 and SP 550 filters (Comar). For OH LIF, the frequency-doubled output from one dye laser was tuned near 283 nm to excite the $Q_1(6)$ line in the $A^2\Sigma^+$–$X^2\Pi(1,0)$ band. The frequency-doubled output from the second dye laser was tuned to pump the peak of overlapping transitions in the A^1A_2–$X^1A_1 4^1{}_0$ band of CH_2O near 353 nm. Further details of the experimental procedure are given by Ayoola *et al* (2006).

3. Image analysis

3.1. Image preprocessing

The raw fluorescence images were preprocessed to reduce noise by use of a median filter. The resulting filtered images were normalized by the laser sheet intensity profiles. A warping algorithm was then used to map the pixel coordinates in the filtered OH images onto the corresponding pixel locations in the CH_2O images. This involved taking an image of a test pattern with both cameras and applying a geometrical transformation to one of the test images, using the reference points in the other image as anchor coordinates. After transformation, the Sobel edge detection algorithm (Vernon 1991) was applied to the OH PLIF images to create the flame contour. The resulting flame contour is a line composed of contiguous square pixels each with a size of 70 μm.

3.2. Curvature evaluation

The pixelated flame contour is the basis by which planar curvature can be measured. Various methods of evaluating curvature from the contour exist; the most basic way involves evaluating curvature directly from the pixel coordinates (Nye *et al* 1996, Ayoola *et al* 2006). This results in a poor estimation of the spatial second derivatives used in the computation of curvature, which are sensitive to the effects of pixelation noise. Pixelation noise results from the approximation of the true coordinates of the curve to the nearest pixel within the pixel matrix. The unpredictable influence of pixelation can be envisaged as introducing random noise to the representation of the real continuous curve. To minimize this effect, the pixelation noise is filtered to obtain an approximately continuous coordinate representation.

In the present work, this filtering is performed by local fitting of a polynomial curve of specified length and specified degree to a sequence of adjacent pixels on the flame contour surrounding a central pixel at which the curvature is to be evaluated (Kostiuk *et al* 1999, Shy *et al* 1999, Renou *et al* 2000, Haq *et al* 2002, Soika *et al* 2003). Each locally fitted curve is pivoted at its central coordinate, and has an equal number of curve-fitting points on either side. A local least-square fit of the curve to the discretized points is performed to produce the polynomial coefficients of the 'best fit' curve, hence resulting in an analytical expression for the locally fitted curve. Differentials of x and y with respect to the curvilinear coordinate, s, can then be computed for the subsequent estimation of planar curvature, κ, at the locally fitted polynomial's central pixel (see equation (1)). This process of curve fitting and curvature evaluation is repeated for every point along the flamefront contour:

$$\kappa = \frac{\frac{\mathrm{d}x}{\mathrm{d}s}\frac{\mathrm{d}^2y}{\mathrm{d}s^2} - \frac{\mathrm{d}y}{\mathrm{d}s}\frac{\mathrm{d}^2x}{\mathrm{d}s^2}}{\left[\left(\frac{\mathrm{d}x}{\mathrm{d}s}\right)^2 + \left(\frac{\mathrm{d}y}{\mathrm{d}s}\right)^2\right]^{3/2}}. \tag{1}$$

3.3. Polynomial testing

For accurate curve fitting the length and degree of the polynomial segment must be carefully selected. Polynomials of an insufficient length will imprecisely estimate curvature when fitted to the flame contour, since pixelation noise predominates. Conversely, an excessively long polynomial curve often results in an inaccurate fit that smoothens undulations of the flame contour, and hence consistently underestimates curvature.

Tuning of the curve-fitting parameters can be achieved using an analytical curve, which is then pixelated and fitted

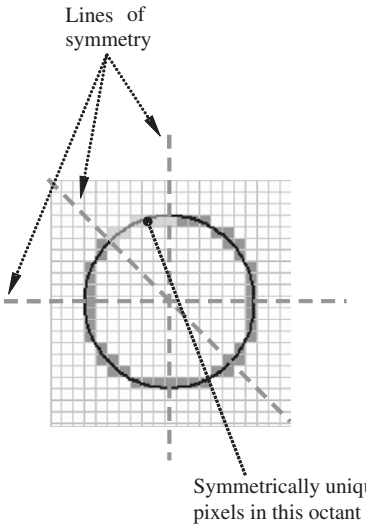

Figure 2. Representation of pixelation and lines of symmetry.

with polynomials, so that the theoretical and the measured curvatures can be obtained; these values are then compared at every point along this test curve. The difference between the theoretical and measured curvatures at every point is then evaluated to compare the errors resulting from different types of polynomial segments. To ensure that the curvature evaluation algorithm will measure curvature of a pixelated flame contour with a minimal error over the curvature range of interest, the test curve should possess a similar range of curvatures.

Currently, no systematic method of tuning the two parameters for polynomial curve-fitting exists. A simple test case involving circles of various radii has been used, for example, by Haq *et al* (2002). Unfortunately, the circle, which has a fixed theoretical curvature, does not realistically represent the undulating nature of a typically contorted flamefront, which changes both sign and magnitude in curvature. A further problem is that the circle has symmetry such that there are eight octants that are pixelated identically, as illustrated in figure 2. This means that only the pixels of one octant of the circle are 'symmetrically unique' (i.e., pixels with their centres that are uniquely offset from the underlying theoretical curve, see figure 2). Each symmetrically unique pixel has a unique value for the curvature measured at its location by use of polynomial fitting, which differs from the theoretical curvature due to the effects of aliasing.

In order to compare the effectiveness of different sets of tuning parameters, we must evaluate, for each theoretical curvature, the sample mean of the absolute offset between the measured and theoretical curvatures over all the symmetrically unique pixels in the test object (i.e., over one octant of the circle). If there are too few symmetrically unique pixels, then the sample mean does not represent a good estimation of the mean that would be found with a much larger number of symmetrically unique pixels. This leads to difficulties when performing polynomial testing at higher curvatures using test circles because small test circles have fewer pixels that are symmetrically unique. The circular test case would hence not necessarily offer an accurate basis upon which to tune the curvature evaluation algorithm for measuring curvature from flame contours.

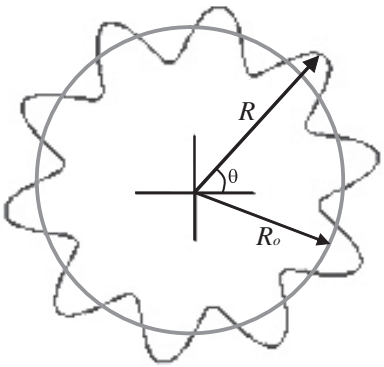

Figure 3. An example test rosette for a given set of parameters, where $A = 0.3R_o$ and $B = 10$.

An alternative method for curvature algorithm testing, referred to as the 'rosette test curve' herein, was conceived, in order to improve upon circular test curves, which is best expressed in polar coordinates, given by

$$R = R_o + A\sin(B\theta) \tag{2}$$

where

$$A \leqslant R_o, \quad B \in \mathbb{Z}^+ \quad \text{and} \quad 0 \leqslant \theta < 2\pi.$$

Here, R_o is the mean radius about which R oscillates and A is the amplitude of oscillation, with the constraint that B only adopts positive integers. A plot of an example test rosette is shown in figure 3.

This test curve formulation yields a continuous curve with a cyclically repetitive pattern. The utility of this curve is based upon its periodic elements being repeated in different orientations relative to the rectangular grid of pixels, consequently yielding slightly dissimilar pixelated shapes of the elements. This random distorting effect of pixelation upon the measured curvature for the test curve means that all of the pixels are symmetrically unique; this is paramount for reliably tuning the curve-fitting parameters. The rosette test curve also has the advantage of a variation of theoretical curvature along the contour and an alternation of curvature sign, which more realistically represents the undulating nature of a flame contour than the circular test curve.

Polynomial testing involves computing the theoretical and measured curvatures at each point on the rosette curve. The absolute value of the difference between the theoretical and measured curvatures is then calculated for each point. The data are then binned in terms of theoretical curvature, and for each bin (of width $\Delta\kappa_i$) the arithmetic mean of the absolute offset between measured and theoretical curvature is determined, denoted by δ_i. The polynomial order and length chosen results from the smallest value of the mean offset ($\bar{\delta}$) over the range of curvatures $\left(\kappa_{n_{\text{bins}}} - \kappa_1\right)$ present in the flame under study, given by the minimization with respect to the order and length of the polynomial:

$$\min_{\text{order,length}} \left\{ \bar{\delta} = \frac{1}{\kappa_{n_{\text{bins}}} - \kappa_1} \sum_{i=1}^{n_{\text{bins}}} \delta_i \cdot \Delta\kappa_i \right\}. \tag{3}$$

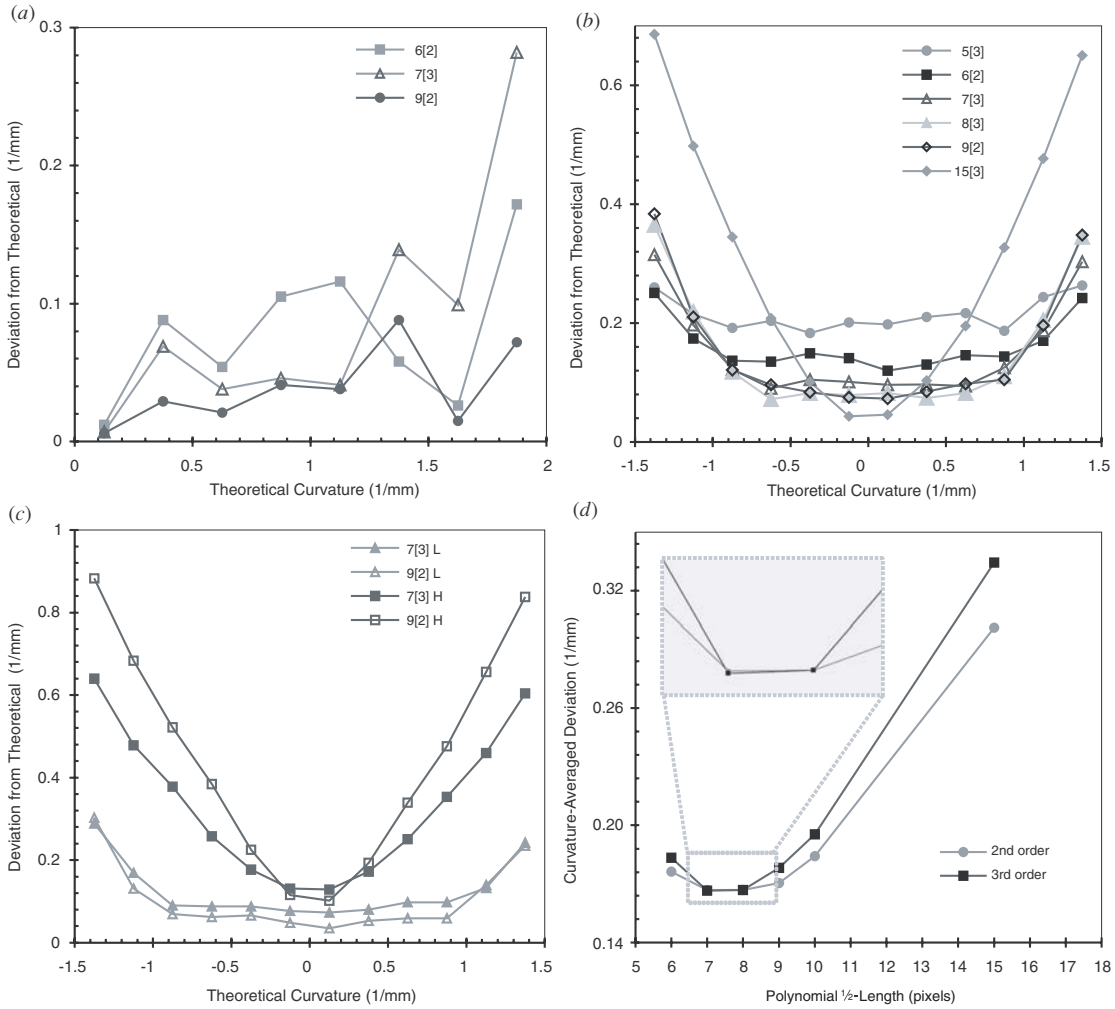

Figure 4. Bin-averaged absolute deviations from the theoretical curvature for (*a*) the circle test and (*b*)–(*c*) the rosette test. Note: 7[3] denotes a third-order polynomial of half-length 7 pixels. *L* and *H* denote the low and high maximum curvilinear rates of change of curvature of 2 and 6 mm^{-2}, respectively. (*d*) Curvature-averaged absolute deviations from the theoretical curvature for the rosette test.

A range of rosette shapes was used as a basis for polynomial testing; this was performed by setting the three parameters A, B and R_o in the rosette formulation, so that the maximum absolute curvature along the rosette was fixed to 1.5 mm^{-1} for all the test curves used here. This value was chosen to roughly match the highest curvatures that were encountered in the flame contours studied. Furthermore, the curvilinear rate of change of curvature ($\mathrm{d}\kappa/\mathrm{d}s$) was computed. In general, this parameter is also important in characterizing the shape of a contour and the ability of curvature to be resolved properly from its constituent pixels. In order to investigate the effect of this shape-defining parameter on the choice of suitable polynomial, a range of maximum absolute values of $\mathrm{d}\kappa/\mathrm{d}s$, that are present at the extremely contorted points on the test curve, were used in this investigation ranging from 2 to 6 mm^{-2}.

3.4. A measure of laminar burning speed

Once the curvature evaluation algorithm had been tested with various polynomials, it was applied to the flame contours, derived from the HRR images, in order to compute curvature. A quantity proportional to the local integrated rate of burning was also computed by integrating the heat release rate profile orthogonal to the flame contour. The integrated result has been suggested to be directly proportional to the laminar flame speed (Warnatz *et al* 1996):

$$S_L = \frac{1}{\rho_{\mathrm{dens}} Y_{\mathrm{fuel}}} \int_{-\tau/2}^{\tau/2} w_{\mathrm{local}}\, \mathrm{d}s, \tag{4}$$

where ρ_{dens} is the fuel mixture density, Y_{fuel} is the fuel mass fraction, τ is the flame thickness and w_{local} is the rate of burning per unit volume. This then allows experimentally obtained correlations between the curvature in the image plane and the local integrated heat release rate to be compared to correlations between flame curvature and laminar flame speed obtained from computational modelling.

4. Results and discussion

4.1. Polynomial testing results

Figure 4 shows three graphs of the arithmetic mean of the absolute deviation from theoretical curvature against

theoretical curvature and demonstrates how these relationships predominantly depend upon polynomial length. Each data-point in figure 4 represents the mean value of absolute deviation within a curvature bin, whose width is 0.25 mm^{-1}. Figure 4(*a*) shows that the curvatures computed by applying a second-order locally fitted polynomial of half-length 9 pixels (denoted as 9[2]) to a series of test circles yields the smallest deviation almost consistently out of all the possible polynomial types that were studied. It should be noted that the three plots shown are only a small selection of the large number of polynomial types studied; this is to preserve graphical clarity. Application of 6[2] polynomials to the test circles yields a low overall deviation compared to other possible choices, however it is seemingly outperformed by polynomial 9[2].

Figure 4(*a*) suggests that a common underlying trend between absolute deviation and theoretical curvature exists for all polynomial types, such that deviation increases with higher curvature. This is expected because the fitting of polynomials to smaller circles leads to poorer fits to the circle's pixels; this results in spatial averaging, which causes underestimations of the true curvature. Furthermore, the trends for the three polynomials in figure 4(*a*) become more erratic with increasing curvature. There is a decrease in consistency between the three trends for curvatures greater than about 1 mm^{-1}, which is due to the higher level of uncertainty present in the measured curvatures associated with smaller circles. As discussed in section 3.3, larger uncertainties exist in the averaged deviations for smaller circles, because fewer values are used in the computation of the average; this is the case as smaller circles have fewer symmetrically unique pixels upon which to form an unbiased average.

Figure 4(*b*) shows the results from applying five polynomial types to a test rosette that was set with a maximum absolute curvature of 1.5 mm^{-1} and a maximum absolute curvilinear rate of change of curvature of 3 mm^{-2} along its profile, whose values are a realistic range present within the flame contours studied here. Figure 4(*b*) shows similar underlying trends to that of the results from the circle tests, in that deviation from true curvature increases with higher absolute curvature due to the increase in spatial averaging. There is a little scatter in the data in the curves of figure 4(*b*) unlike for the circle test results in figure 4(*a*). The smoother plots result from a smaller uncertainty in the average measured curvatures from the test rosette. This is the case because the test rosette used in this example was set with a large radius, R_o, which generated a large number of repeating segments; this results in the segments lying in many different locations relative to the rectangular matrix of pixels. Consequently, each point in figure 4(*b*) represents an average over data obtained from a large number of symmetrically unique pixels.

Upon measuring curvatures on the rosette for a given theoretical curvature, the average deviation (within a bin) between measured and theoretical curvature can be estimated from a significantly larger number of periodically repeated points upon the rosette when R_o is large, in contrast to the small number of repeated points using circle testing with high-curvature small circles. A rosette with a larger radius, R_o, results in a larger circumference, which can accommodate many more repetitions of the periodic segments of the rosette; this results in larger statistical confidence within the bin-averaged curvatures.

A set of similar polynomial types exists that each yields very similar deviations from the theoretical curvature, as shown in figure 4(*b*) for that rosette test curve; these include polynomials 7[3], 8[3] and 9[2]. However, polynomials of appreciably different lengths, such as 5[3] and 15[3] in this case, yield significantly larger overall deviations. For the case of too short a polynomial, large deviations exist across all values of theoretical curvature, as demonstrated in case 5[3] by its flat profile. This is caused by the fitting of polynomials with too few points, thus resulting in a larger scatter in the measured curvatures, and hence larger absolute deviation. Overly long polynomials do not suffer from pixelation noise, yet exhibit larger deviations at higher curvatures, because the fitting of long polynomials causes spatial filtering that results in high theoretical curvatures being systematically underestimated.

Although it has been seen that there is a group of polynomials with a similar length and degree that each yields very similar levels of small deviation from true curvature in figure 4(*b*), this is not the case in general. This has been tested through the use of rosette test curves of different shapes obtained by varying the maximum rates of change of curvature, $(d\kappa/ds)_{max}$. Figure 4(*c*) shows the variation of deviation with curvature for the application of two polynomial types to two test rosettes of different maximum values of $d\kappa/ds$ of 2 mm^{-2} and 6 mm^{-2}. These two rosettes both had the same maximum curvature of 1.5 mm^{-1}, but with different shapes of the rosette, as determined by $(d\kappa/ds)_{max}$. It was found that two polynomial types, 7[3] and 9[2], which give reasonably small deviations for a rosette with a maximum $d\kappa/ds$ of 3 mm^{-2} (as for figure 4(*b*)), do not necessarily yield the same results when applied to curves with different shapes. This is demonstrated in figure 4(*c*), where polynomial 7[3] leads to less overall deviation than 9[2] for nearly all curvatures throughout the rosette with a higher maximum rate of change of curvature. Conversely, 9[2] yields slightly less overall deviation than 7[3] for the rosette with lower maximum rate of change of curvature for all curvatures of interest in this study (i.e., $-1.5 < \kappa < 1.5$ mm^{-1}). Figure 4(*c*) suggests that increasing the maximum value of $(d\kappa/ds)_{max}$ increases the minimum deviation that occurs at zero curvature, and there is an accompanying increase in the sensitivity of deviation to curvature as shown by larger gradients in these plots. It is seen that there is an increase in sensitivity to polynomial choice with an increase in $(d\kappa/ds)_{max}$, as reflected by the larger differences between the profiles for the polynomials 7[3] and 9[2]. In light of these findings, it would thus always be wise to perform preliminary computations to estimate the range of curvatures and of rates of change of curvatures in the contours under study by using an initial guess for a polynomial type and length. This heuristic would then allow the test rosette to be adapted to the appropriate shape, in order to refine the choice of final polynomial length and degree to be used. In this case, the polynomial 7[3] has been chosen for the purpose of calculating curvature within the flame contours, as it has shown to possess the lowest curvature-averaged deviation,

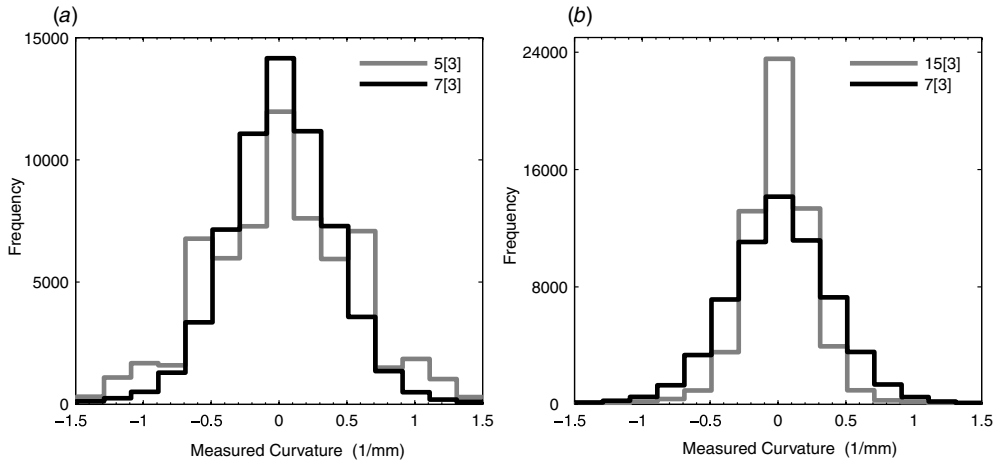

Figure 5. Curvature distributions of the flame with a flow rate of 2.4 m s^{-1} for three polynomial types.

as calculated by equation (3). This result is shown in the enlargement of figure 4(*d*), which shows that 7[3] is the best choice in this case. This result highlights that the choice of 9[2] from the circle test is not suitable, hence demonstrating the utility of the rosette test curve method.

4.2. Application to flame data

4.2.1. Curvature distributions. Figure 5 shows flamefront curvature histograms for the flame with the lowest fuel mixture flow rate of a bulk speed of 2.4 m s^{-1}. The histograms depict differences between the measured-curvature distributions of the flame arising from the use of three polynomials: 5[3], 7[3] and 15[3]. Polynomial 7[3] is a benchmark, as it was shown to yield accurate measurements of curvature from the rosette, as shown in figure 4(*d*). The effects of the other polynomials upon the measured-curvature distribution are also shown.

The shape of the distributions for all polynomials is symmetrical, and each one is centred at zero curvature; this is consistent with the almost planar time-averaged profiles of the flamefront in the counterflow burner. Yet, appreciable differences exist between distributions using the benchmark and the other polynomials. Use of polynomial 5[3] to compute the curvature distribution, as shown by the grey line histogram in figure 5(*a*), leads to a larger spread of curvatures with a 36% increase in the standard deviation relative to the benchmark. The increased spread is attributable to the effects of pixelation noise. The pixelation noise is also considered to cause the greater amount of noise in the distribution, as shown by the peaks at curvatures of -0.6 and 0.6 mm^{-1}.

The use of a larger polynomial, such as 15[3], to measure flamefront curvature leads to a narrower distribution (35% smaller standard deviation) as represented by the grey line histogram in figure 5(*b*). This is due to the systematic underestimation of curvatures by using a long polynomial. These PDF plots thus demonstrate the importance of selecting a suitable polynomial segment length in the evaluation of flamefront curvature.

4.2.2. HRR correlations. Uncertainties in the estimation of curvature have implications for the accuracy of the correlation of integrated HRR with flamefront curvature. Figure 6 shows four graphs of such a correlation: (a), (b) and (c) show plots for the different polynomial types that were investigated for the curvature evaluation algorithm testing. Graph (d) shows the same correlated variables for the suitable polynomial choice (e.g., 7[3]) for the three flames investigated. It should be noted that each data-point in these plots represents the bin-average integrated HRR. Each bin average was determined based on at least 200 individual evaluations of curvature and heat release rate. This avoids the random scatter in the correlation plots that would result from a lack of sufficient data in each bin. The positions along the curvature axis of each point, representing the average HRR within a bin, are based on the centroid of the scattered data within a bin along the curvature axis.

It is clear from figures 6(*a*)–(*c*) that other polynomials such as 8[3] or 9[2] could, for example, have been chosen since they lead to similar correlations. Polynomials 7[3], 8[3] and 9[2] lead to very similar trends with a significant increase in burning rate for negative curvatures.

It is apparent from figure 4(*b*) that an inadequately long polynomial, such as 5[3], would yield a correlation within figure 6 with lower gradients. This is due to short polynomials being more sensitive to pixelation noise, and leads to a larger spread in the curvature distribution. Conversely, for longer polynomials, the HRR correlation is generally steeper due to the tendency to systematically underestimate curvature. It should be noted that for polynomial 15[3], the positive curvature parts of the plots are irregular across figures 6(*a*)–(*c*) and do not show an artificially steep gradient that would be consistent with the left half of the plots. Specifically, it is seen in figures 6(*a*) and (*b*) that the correlation for 15[3] reaches a trough, for instance, which is offset from zero curvature. This behaviour could be attributed to an inaccuracy in the integrated HRR values, due to the direction of integration across the flamefront not being perpendicular to the true flamefront orientation. The direction of integration is governed by the estimates made for the gradients, dx/ds and dy/ds, whose accuracies are determined by the length and degree of the polynomial. As an example, figure 7 portrays a schematic of the least-square best fit of a long polynomial that is centred at a

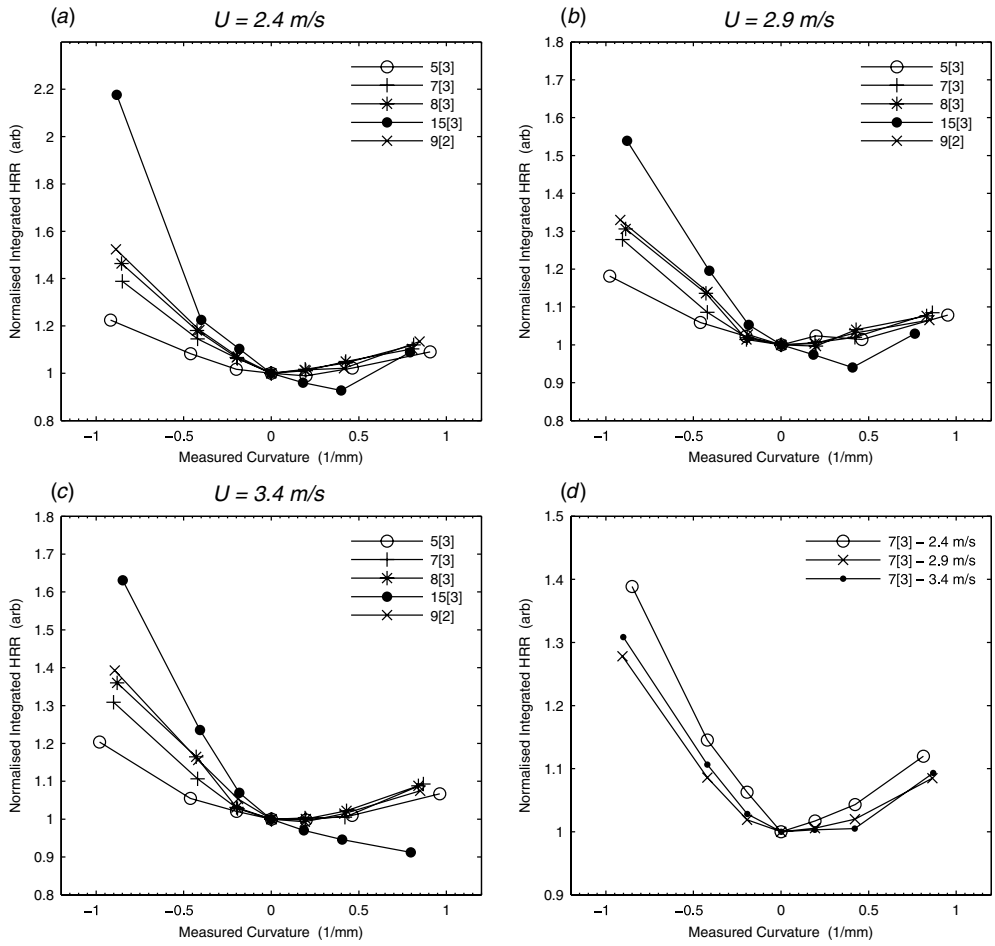

Figure 6. Correlations of integrated HRR with flamefront curvature. Plots (*a*), (*b*) and (*c*) show comparisons between five polynomials for the three flames characterized by flow speeds of 2.4, 2.9 and 3.4 m s^{-1}, respectively. Plot (*d*) shows the correlations for the best choice of polynomial.

point of inflection, as denoted by the superimposed pivot point on the HRR image of a flamefront. Cross-sections 1 and 2 are examples of paths of integration across the flamefront, which are always aligned to the local normal of the polynomial. The accompanying dashed lines, which represent the flamefront's orthogonal, portray the potential for disparities between them and the direction of the integration paths.

A possible reason for the unpredicted lowering of the right half of the 15[3] plots of figures 6(*a*)–(*c*) is based on the following argument. If a polynomial that is pivoted at the flamefront's point of inflection is too long, the least-square best fit to the neighbouring pixels does not provide an appropriate path for integration across the flamefront, as shown by integration path 1 in figure 7. This will always lead to overestimation of the true integrated HRR values across the flamefront. However, for regions of the flamefront with a higher magnitude curvature, the path lengths for integration are perpendicular to the flame contour, as would be found from a polynomial fitted around position 2 in figure 7. Consequently, this effect raises the integrated HRR values at zero curvature, relative to the higher magnitude curvatures. Once the plot for the overly long polynomial is normalized by this larger integrated HRR value at zero curvature, the curve is shifted downward relative to the correlations based on more

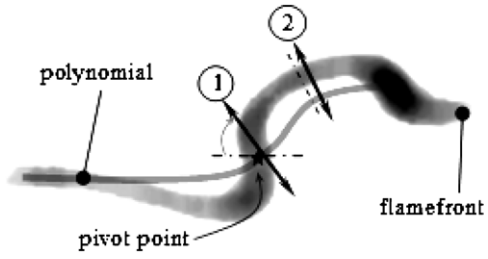

Figure 7. Schematic of the fitting of an overly long polynomial to an HRR-based image of a flamefront with the associated HRR-integration paths 1 and 2.

appropriate polynomials, thus contributing to the lowering of the right-hand section of the plot.

4.2.3. Physical effects. Figure 6(*d*) displays the correlations of local integrated HRR with flamefront curvature for a choice of polynomial 7[3] for all three flames with bulk flow speeds of 2.4, 2.9 and 3.4 m s^{-1}. It is seen that for the three flames there is a significant increase in burning rate, which is proportional to integrated HRR, with increasing magnitude of negative curvature and a less strong increase in burning rate with increasing positive curvature. These results concur

with the correlations obtained from numerical simulation by Chakraborty and Cant (2005) for lean methane/air $Le = 1.2$ flames. In these theoretical studies, a bivariate PDF was also found to exhibit both a strong increase in the reaction component of flame displacement speed (i.e., S_r) with decreasing negative curvature and a smaller increase in S_r with increasing positive curvature. Rutland and Trouvé (1993) predicted similar behaviour for a lean methane/air $Le = 1.2$ flame, for negative curvatures, although correlations from their numerical simulations showed no noticeable increase in burning rate for positive curvatures.

A possible reason for the shape of the correlations is the thermodiffusive argument put forth by Williams (1986). The flamefront diffusion of heat from the burnt gases towards the incoming reactants takes place at the same time as the fuel within the reactants diffuses towards the flamefront. When the flamefront is curved this causes the diffusive flux of heat to focus (defocus) at the flamefront regions concave (convex) to the reactants, whilst the diffusive flux of fuel defocuses (focuses) at the concave (convex) regions. For the case of the concave region, the focusing of heat is conducive to locally increasing the temperature of the unburnt fuel mixture close to the flamefront and hence raises the local rate of reaction. However, the defocusing of the fuel diffusion towards the flamefront in concave regions tends to reduce the concentration of fuel close to the flamefront. It is postulated that the two effects compete and hence the balance between them determines the relationship between local integrated heat release rate and the curvature of the flamefront. Moreover, the balance of these two effects can be skewed by the global Lewis number, Le, which is defined as the ratio of the thermal diffusivity of the fuel–air mixture to the binary mass diffusivity of the fuel in nitrogen at inlet conditions. When the thermal diffusivity is greater than the mass diffusivity (i.e., $Le > 1$) the effect of the focusing (or defocusing) of heat is more important than that of fuel diffusion effects, and thus it would be seen that concave regions of the flamefront would exhibit a higher integrated heat release rate than its convex neighbours.

Nevertheless, there are limitations to the interpretations of figure 6(*d*), because of the correlation of burning rate with flamefront curvature that is measured only in two dimensions. The real flame surface requires two components of curvature to fully characterize its topological profile in three dimensions. This fact implies that quantification of the relative enhancements of burning for the negative curvatures should not be trusted entirely. It would be expected that the correlation of true curvature with the burning rate would exhibit a stronger enhancement of burning for negative curvatures, when compared with the correlations of figure 6(*d*). This is exemplified by the correlations of Chakraborty and Cant (2005), where they use mean curvature (κ_m) as a measure of flame surface contortion, that show gradients for the negative curvatures in their correlation to be double that of figure 6(*d*). A more uniform correlation would be expected for burning rate with a two-dimensional curvature (κ) because for each of the measured curvatures herein there would have been an associated curvature in the direction perpendicular to the laser sheet. For example, a strong curving of the flame surface could exist out of the measuring plane, yet would appear to be flat in the HRR images of the flamefront, which results in an enhancement for zero curvatures in the correlations of figure 6. This would result in larger burning rates for zero curvatures relative to that for negative curvatures, hence a levelling of the correlation.

5. Conclusions

An improved method for the computation of a two-dimensional curvature and its application to turbulent premixed flame correlations has been developed and tested in this study. It has been shown that use of a circle as a test curve for tuning the parameters of the curvature evaluation algorithm does not reliably yield the best choice of polynomial type. The rosette test curve method, whose development is reported here, was shown to perform more effectively, and to consistently allow the selection of an appropriate polynomial for smoothing the pixelated flame contour.

A problem of the circle as a test curve is that its symmetry causes only one octant to possess pixels that are symmetrically unique. This leads to problems when investigating high curvatures since for the corresponding small circles there will be very few unique pixels. Furthermore, employing the rosette test curve allowed for the setting of the maximum curvilinear rate of change of curvature $(\mathrm{d}\kappa/\mathrm{d}s)_{\max}$ that occurs along the contour, which is, however, undefined for circle test curves. This extra degree of freedom enabled the effect of $(\mathrm{d}\kappa/\mathrm{d}s)_{\max}$ upon the choice of suitable polynomial to be studied. It was found that curves with larger $(\mathrm{d}\kappa/\mathrm{d}s)_{\max}$ exhibit larger sensitivity of curvature measurement accuracy to the choice of polynomial.

For the irregularly distorted flame contours investigated, a group of polynomial types was found to yield very similar results for the rosette testing performed. Furthermore, application of this group of polynomials yielded very similar correlations of burning rate with flamefront curvature, thus supporting the fidelity of the rosette testing results. Further to the predictable effects of polynomial length upon the distribution of measured curvatures, whereby shorter polynomials yield wider distributions and longer polynomials tend to smoothen the undulating flame contour, longer polynomials also seemed to lead to distortions to the true underlying relationship between local integrated HRR and flamefront curvature. This distortion is suspected to be due to systematic errors present in the values of integrated HRR due to the use of overly long polynomials, which can lead to a systematic overestimation of HRR due to inaccurate identification of the direction normal to the flamefront.

Finally, qualitative agreements were found between the experimental correlations reported here and the behaviour that would be expected based on the thermodiffusive argument, in addition to the DNS results within the literature.

Acknowledgments

We thank B Ayoola for provision of his experimental datasets and many useful discussions. This work was sponsored by the EPSRC under grant EP/F028261/1, and by Rolls-Royce plc.

RSMC was supported by an EPSRC CASE studentship, whose contributions are gratefully acknowledged. ISB was supported by a research fellowship from St. John's College, Cambridge, UK. CFK gratefully acknowledges personal sponsorship from the Leverhulme Trust, and JH acknowledges support by an advanced research fellowship (EP/C012399/1) from the EPSRC.

References

Ayoola B O, Balachandran R, Frank J H, Mastorakos E and Kaminski C F 2006 Spatially resolved heat release rate measurements in turbulent premixed flames *Combust. Flame* **144** 1–116

Chakraborty N and Cant R S 2005 Influence of Lewis number on curvature effects in turbulent premixed flame propagation in the thin reaction zones regime *Phys. Fluids* **17** 105105

Chen Y C 2007 Measurements of flame-front curvature based on Fourier transformation *Combust. Theor. Model.* **11** 333–49

Gashi S, Hult J, Jenkins K W, Chakraborty N and Cant R S 2005 Curvature and wrinkling of premixed flame kernels—comparison of OH PLIF and DNS data *Proc. Comb. Inst.* **30** 809–17

Haq M Z, Sheppard C G W, Woolley R, Greenhalgh D A and Lockett R D 2002 Wrinkling and curvature of laminar and turbulent premixed flames *Combust. Flame* **131** 1–115

Kaminski C F 2005 Fluorescence imaging of reactive processes *Z. Phys. Chem* **219** 747–74

Kostiuk L W, Shepherd I G and Bray K N C 1999 Experimental study of premixed turbulent combustion in opposed streams. Part III—spatial structure of flames *Combust. Flame* **118** 129–39

Law C K 1988 Dynamics of stretched flames *Proc. Comb. Inst.* **22** 1381–402

Lee S H and Chen I C 1996 Axis switching in the $\tilde{B}^2A'$–$\tilde{X}^2A'$ transition of HCO and fluorescence lifetimes of the $\tilde{B}^2A'(0, 0, 0)$ rotational states *J. Chem. Phys.* **105** 2583–90

Mantel T and Samaniego J 1999a Fundamental mechanisms in premixed turbulent flame propagation via vortex flame interactions Part I: experiment *Combust. Flame* **118** 537–56

Mantel T and Samaniego J 1999b Fundamental mechanisms in premixed turbulent flame propagation via vortex flame interactions Part II: numerical simulation *Combust. Flame* **118** 557–82

Mastorakos E, Taylor A M K P and Whitelaw J H 1992 Extinction and temperature characteristics of turbulent counterflow diffusion flames with partial premixing *Combust. Flame* **91** 40–54

Najm H N, Paul P, Mueller C and Wyckoff P S 1998 On the adequacy of certain experimental observables as measurements of flame burning rate *Combust. Flame* **113** 312–32

Nottin C, Knikker R, Boger M and Veynante D 2000 Large eddy simulations of an acoustically excited turbulent premixed flame *Proc. Comb. Inst.* **28** 67–73

Nye D A, Lee J G, Lee T W and Santavicca D A 1996 Flame stretch measurements during the interaction of premixed flames and Kármán vortex streets using PIV *Combust. Flame* **105** 167–79

Öttinger H 2005 *Beyond Equilibrium Thermodynamics* (New York: Wiley)

Paul P and Najm H N 1998 Planar laser induced fluorescence imaging of flame heat release rate *Proc. Comb. Inst* **27** 43–50

Pitsch H 2006 Large-eddy simulation of eddy combustion *Ann. Rev. Fluid Mech.* **38** 453–82

Renou B, Boukhalfa A, Peuchberty D and Trinité M 2000 Local scalar flame properties of freely propagating premixed turbulent flames at various Lewis numbers *Combust. Flame* **123** 507–21

Rutland C J and Ferziger J 1991 Simulations of flame-vortex interactions *Combust. Flame* **84** 343–60

Rutland C J and Trouvé A 1993 Direct simulations of premixed turbulent flames with non-unity Lewis numbers *Combust. Flame* **94** 41–57

Shy S S, I W K, Lee E I and Yang T S 1999 Experimental analysis of flame surface density modelling for premixed turbulent combustion using aqueous autocatalytic reactions *Combust. Flame* **118** 606–18

Soika A, Dinkelacker F and Leipertz A 2003 Pressure influence on the flame front curvature of turbulent premixed flames: comparison between experiment and theory *Combust. Flame* **132** 451–62

Vernon D 1991 *Machine Vision* (Englewood Cliffs, NJ: Prentice-Hall)

Veynante D and Vervisch L 2002 Turbulent combustion modelling *Prog. Energy Combust. Sci.* 193–266

Warnatz J, Mass U and Dibble R W 1996 *Combustion* (Berlin: Springer)

Williams F A 1986 *Combustion Theory: The Fundamental Theory of Chemically Reacting Flow Systems* (Reading, MA: Addison-Wesley)